

Bridging Function Approximation and Device Physics via Negative Differential Resistance Networks

Songyuan Li^{1†}, Teng Wang^{1†}, Jinrong Tang¹, Ruiqi Liu¹, Yuyao Lu², Feng Xu², Bin Gao², Xiangwei Zhu^{1*}

^{1*}School of Electronics and Communication Engineering, Sun Yat-sen University, Shenzhen, 518107, China.

²School of Integrated Circuits, Innovation Center for Future Chips, Tsinghua University, Beijing, 100084, China.

*Corresponding author(s). E-mail(s): zhuxw666@mail.sysu.edu.cn;

†These authors contributed equally to this work.

Abstract

Achieving fully analog neural computation requires hardware that can natively implement both linear and nonlinear operations with high efficiency. While analogue matrix-vector multiplication has advanced via compute-in-memory architectures, nonlinear activation functions remain a bottleneck, often requiring digital or hybrid solutions. Inspired by the Kolmogorov-Arnold framework, we propose KANalogue, a fully analogue implementation of Kolmogorov-Arnold Networks (KANs) using negative differential resistance devices as physical realizations of learnable univariate basis functions. By leveraging the intrinsic negative differential resistance characteristics of tunnel diodes fabricated from NbSi₂N₄/HfSi₂N₄ heterostructures, we construct coordinate-wise nonlinearities with distinct curvature and support profiles. We extract I-V data from fabricated armchair and zigzag devices, fit high-order polynomials to emulate diode behavior in software, and train KANs on vision benchmarks using these learned basis functions. Our results demonstrate that KANalogue can approximate complex functions with minimal parameters while maintaining classification accuracy competitive with digital baselines. This work bridges device-level physics and function approximation theory, charting a path toward scalable, energy-efficient analogue machine learning systems.

Keywords: Analogue In-Memory Computing, Negative Differential Resistance, Kolmogorov-Arnold Network

1 Introduction

The growing demand for efficient machine learning on edge devices has intensified the search for alternatives to conventional digital architectures, which often struggle with power and latency constraints [1, 2]. Neuromorphic computing offer a compelling pathway, exploiting device physics to achieve orders-of-magnitude

gains in energy efficiency and computational density [3, 4]. Recent advances in analogue in-memory computing (AIMC) based on resistive RAM (RRAM) and phase-change memory (PCM) have demonstrated near-software-level accuracy for large-scale matrix-vector multiplication [5–13]. By leveraging Ohm’s law and Kirchhoff’s current law, AIMC arrays physically co-locate

memory and computation to perform these linear operations *in situ*, directly alleviating the von Neumann bottleneck that arises from shuttling data between separate memory and processing units [14–16]. Yet neural networks are not purely linear systems: they rely on alternating linear and nonlinear transformations. A critical obstacle remains because most analogue accelerators still delegate nonlinear activation functions to digital circuits, breaking the vision of fully analogue neural pipelines and limiting overall efficiency [5, 17].

Kolmogorov–Arnold Networks (KANs) provide a unique opportunity to address this gap. Inspired by the Kolmogorov–Arnold superposition theorem [18], KANs replace edge weights with learnable coordinate-wise basis functions. This structural distinction shifts expressive capacity from dense matrix multiplication to univariate nonlinear transformations, enabling compact models that differ fundamentally from traditional multilayer perceptrons [19]. Crucially, it also makes KANs particularly suitable for analogue realization: each basis function can, in principle, be instantiated directly by a physical nonlinear device. Combined with their reduced parameter counts compared to conventional networks, KANs offer a smaller hardware footprint and lower energy demands. Recent variants have been applied to symbolic regression [20], modeling of physical systems [21–23], remote-sensing image classification [24], and molecular property prediction [25]. Despite these advantages, KANs have so far been realized only in digital or hybrid platforms [26, 27], leaving their analogue potential largely unexplored.

Nonlinear devices with negative differential resistance (NDR) offer a promising route to close this gap. Esaki diodes [28], resonant tunneling diodes [29, 30], and recently designed cold-metal devices [31, 32] naturally exhibit nonlinear current–voltage characteristics that resemble activation functions. Prior work has demonstrated the use of NDR devices to implement spiking neurons [33], bistable logic gates [34], or to emulate software-defined nonlinearities in memristor crossbars [17]. However, integrating device-level nonlinearities directly into function-based architectures has yet to be realized.

Here we introduce KANalogue, a framework that implements Kolmogorov–Arnold Networks using NDR devices as physical instantiations of univariate basis functions. NDR devices exhibit inherently nonlinear, non-monotonic current–voltage characteristics that provide rich expressive capability. Moreover, multiple NDR elements can be composed to realize more complex nonlinear functions, further extending the representational capacity of analogue nodes. This property allows KAN nodes to approximate complex mappings with fewer units, improving node efficiency and enabling more compact network realizations. By mapping these device characteristics to the functional components of KANs, KANalogue establishes a direct bridge between quantum electronic behavior and neural computation. Through simulation and surrogate modeling based on cold-metal tunnel diodes, we demonstrate that NDR-enabled KANs achieve competitive accuracy on standard benchmarks while reducing parameter counts and eliminating digital nonlinearity computation. When scaled to larger systems, such analogue implementations naturally exhibit statistical robustness: variations and noise across individual devices are averaged out through distributed computation, imparting a degree of error tolerance to the overall network. This work integrates theoretical function approximation with device-level physics, pointing toward scalable, fully analogue neural networks grounded in emerging, manufacturable device technologies.

2 Method

2.1 Tunnel Diodes Simulations

For the device modeling, we constructed atomically thin heterostructures in which NbSi₂N₄ monolayers serve as the electrodes and a HfSi₂N₄ monolayer acts as the tunnel barrier. Both arm-chair and zigzag orientations were considered, and barrier thicknesses of 15 Å and 21 Å were tested to examine orientation- and geometry-dependent transport. A vacuum spacing of 20 Å was added in the out-of-plane direction to eliminate spurious interactions between periodic replicas. These geometries were subsequently used as input for first-principles calculations.

The cold mental tunnel diodes are designed To calculate the I–V characteristics, we performed first-principles calculations using DFT within the linear combination of atomic orbitals (LCAO) approach. A double-zeta polarized basis set and norm-conserving FHI pseudopotentials were employed. The exchange-correlation energy was treated using the Perdew–Burke–Ernzerhof (PBE) form of the generalized gradient approximation (GGA). The self-consistent DFT calculations are performed using a $24 \times 24 \times 1$ k-point grid with a density mesh cut-off of 45 Hartree and the total energy converged to at least 10^{-4} Hartree. To eliminate spurious interactions between periodic images, a vacuum spacing of 20 Å was added in the out-of-plane direction.

Transport properties were computed using DFT in combination with the nonequilibrium Green’s function (NEGF) formalism. The DFT-NEGF calculations utilized a $24 \times 1 \times 184$ k-point grid for the armchair orientation and a $14 \times 1 \times 318$ grid for the zigzag orientation of the lateral tunnel diodes. The current-voltage (I–V) characteristics were evaluated using the Landauer formula:

$$I(V) = \frac{2e}{h} \int T(E, V) [f_L(E, V) - f_R(E, V)] dE \quad (1)$$

where $T(E, V)$ denotes the transmission coefficient, and f_L, f_R are the Fermi-Dirac distributions of the left and right electrodes, respectively. A temperature of 300 K was maintained throughout all calculations. Besides, to improve the band gap of the tunnel barrier HfSi_2N_4 , we employed a PBE+U method with a U value of 8 eV for the d orbitals of Hf in the transport calculations.

2.2 Kolmogorov–Arnold Network architecture with tunnel-diode basis functions

To construct the neural architecture, we implemented a variant of Kolmogorov–Arnold Networks (KANs) that replaces the conventional spline- or polynomial-based basis functions with nonlinear responses derived from tunnel-diode current–voltage (I–V) characteristics. Each KAN layer maps an input vector $x \in \mathbb{R}^{d_{\text{in}}}$ to an output vector in $\mathbb{R}^{d_{\text{out}}}$ by first normalizing the inputs using a sigmoid function to ensure they fall within the dynamic range of the diode-based basis functions.

For each input dimension i , a set of tunnel-diode basis functions $\{\phi_k(x_i)\}_{k=1}^K$ is evaluated, where each $\phi_k(\cdot)$ corresponds to either a piecewise polynomial fit of the diode I–V response or an auxiliary bias-like term. These basis functions capture the nonlinear device characteristics obtained from density functional theory (DFT) and nonequilibrium Green’s function (NEGF) simulations. The outputs of these functions are then linearly combined through a trainable coefficient tensor $\Theta \in \mathbb{R}^{d_{\text{in}} \times d_{\text{out}} \times K}$. The layer output is computed as

$$y_j = \sum_{i=1}^{d_{\text{in}}} \sum_{k=1}^K \Theta_{i,j,k} \phi_k(x_i), \quad (2)$$

which corresponds to a learnable superposition of device-inspired nonlinear transformations. This computation is efficiently implemented using Einstein summation notation in PyTorch as

```
y = torch.einsum(
    "bid,ioid->bo", TD_basis, coeffs)
```

where TD_basis stores the evaluated tunnel-diode basis functions for all inputs in the batch.

To capture device-level variability, we further introduced an optional Gaussian perturbation of the coefficients during training:

$$\tilde{\Theta}_{i,j,k} = \Theta_{i,j,k} + \epsilon, \quad \epsilon \sim \mathcal{N}(0, \sigma^2), \quad (3)$$

which emulates fabrication-induced fluctuations in physical implementations.

At the network level, we constructed multi-layer tunnel-diode KANs by sequentially stacking the above layers. Intermediate LayerNorm operations were included to stabilize activations. For image classification tasks, such as MNIST and Fashion-MNIST, the input images were first flattened and normalized before being passed into the first tunnel-diode KAN layer. The final layer produced a 10-dimensional output corresponding to the class logits. While deeper architectures can be employed, we observed that a two-layer TD-KAN already achieves competitive performance on simple benchmarks, whereas larger datasets such as CIFAR-10 highlight the scalability limitations of the current approach.

Dataset preprocessing.

Prior to training and evaluation, all datasets were preprocessed to ensure compatibility with the tunnel-diode KAN architecture and to improve training stability. For MNIST, the grayscale images were resized to 14×14 pixels to reduce the input dimensionality, converted to tensors, and optionally rescaled such that pixel intensities fell within $[0, 2.5]$. In some experiments, we further normalized the data to zero mean and unit variance using the standard MNIST statistics (mean 0.1307, std 0.3081).

For Fashion-MNIST, images were resized to 28×28 pixels, with the same rescaling and optional normalization as in MNIST.

For CIFAR-10, we applied common data augmentation techniques to improve robustness, including random cropping with 4-pixel padding, random horizontal flipping, and color jittering. The images were then normalized to zero mean and unit variance using the standard CIFAR-10 statistics (mean (0.4914, 0.4822, 0.4465) and std (0.2023, 0.1994, 0.2010)).

After preprocessing, the datasets were loaded into mini-batches using `PyTorch DataLoader`, with a batch size of 64 for training and 1024 for evaluation. The final input dimensionalities were $14 \times 14 = 196$ for MNIST, $28 \times 28 = 784$ for Fashion-MNIST, and $3 \times 32 \times 32 = 3072$ for CIFAR-10.

2.3 Comparison

Baseline MLPs with alternative activation functions.

For comparison against tunnel-diode-based KANs, we also implemented multilayer perceptrons (MLPs) in which the conventional nonlinear activation functions were replaced with device-inspired current–voltage (I–V) characteristics. Three activation types were considered: (i) cold-metal tunnel diode, (ii) resonant tunnel diode, and (iii) enhancement-mode MOSFET (E-MOSFET).

Following prior neuromorphic studies [34], the resonant tunnel diode activation function (RTDAF) was modeled using the experimentally

validated I–V characteristic

$$I(V) = a \ln \left(\frac{1 + e^{\alpha + \eta V}}{1 + e^{\alpha - \eta V}} \right) \left[\frac{\pi}{2} + \tan^{-1} \left(\frac{c - n_1 V}{d} \right) \right] + h(e^{\gamma V} - 1), \quad (4)$$

where the physical parameters are defined as $\alpha = \frac{q(b-c)}{k_B T}$, $\eta = \frac{q n_1}{k_B T}$, and $\gamma = \frac{q n_2}{k_B T}$, with q the electron charge, k_B Boltzmann’s constant, T the temperature, and V the applied voltage. In this work we used $T = 300$ K, $a = 0.0039$ A, $b = 0.5$ V, $c = 0.0874$ V, $d = 0.0073$ V, $n_1 = 0.0352$, $n_2 = 0.0031$, and $h = 0.0367$ A, consistent with Ref. [35]. To further explore the nonlinear response, the parameter b was scaled by a factor of ten.

In addition, an E-MOSFET transfer characteristic was employed as an activation function, which resembles a rectified linear unit (ReLU). The functional form is given by

$$I_D = K(V_{GS} - V_{GS(th)})^2, \quad (5)$$

where $K = 6.17$ mA/V² and $V_{GS(th)} = 1$ V, as specified in the datasheet of the 2N7002 E-MOSFET.

The functional forms of all activation types considered—cold-metal tunnel diode, RTDAF, and E-MOSFET—are summarized in Fig. 1. These device-inspired activations provide a consistent framework for evaluating MLP performance against tunnel-diode KANs under different non-linearity choices.

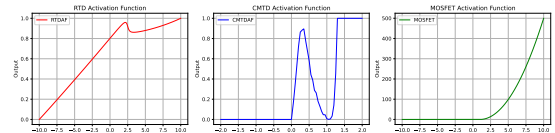


Fig. 1: Activation functions used in MLP baselines: cold-metal tunnel diode, resonant tunnel diode (RTDAF), and E-MOSFET.

3 Results

3.1 Device-level Nonlinearity of Tunnel Diodes

The computational design of the cold metal tunnel diodes is based on density functional theory (DFT) within the QuantumATK U-2022.12 package [36]. The design of lateral NDR tunnel diodes mainly focus on cold metal and semiconducting compounds. We select NbSi₂N₄ as the cold metal electrode and HfSi₂N₄ as the tunnel barrier for the lateral tunnel diode simulations. A kind of the atomic structure, illustrated in Fig. 2, consists of monolayer electrodes sandwiching a monolayer barrier, forming a minimal device unit that naturally exhibits negative differential resistance.

We find that tunnel diodes can exhibit markedly different nonlinear response behaviors depending on their atomic orientation and barrier thickness. In general, the atomic orientation has a pronounced influence on the overall shape of the I–V characteristics, while the barrier thickness primarily affects the magnitude of the current. Specifically, we investigated devices with barrier thicknesses of 21 Å in the armchair orientation, and 21 Å and 15 Å in the zigzag orientation. In addition, we examined a hybrid structure in which the electrodes adopt the zigzag orientation and the barrier layer follows the armchair configuration. The atomic structures’ three-view figure of all investigated tunnel diodes are provided in the Supplementary Information.

To analyze the I–V characteristics of these tunnel diodes, we performed a series of self-consistent transport calculations by sweeping the bias voltage from 0 V to 1.3 V in increments of 0.05 V. As shown in Fig. 4, when the barrier thickness is set to 21 Å, the armchair-oriented device exhibits an N-type negative differential resistance (NDR) effect with a relatively low peak voltage. In contrast, the zigzag-oriented device displays a Λ -type response with a higher peak voltage. Reducing the barrier thickness of the zigzag device to 15 units introduces an additional NDR effect at higher bias voltages. For the hybrid zig–arm–zig configuration, the overall behavior follows the trend of the zigzag structure, although both the peak voltage and the detailed profile show noticeable differences. These observations demonstrate

that variations in atomic structure not only govern the characteristics of the NDR response but also provide different nonlinear behaviors, which may serve as valuable sources of basis functions for KAN architectures.

3.2 Approximating I–V curves with Learnable Functions.

To capture the nonlinear response of the tunnel diodes, we employed both polynomial fitting and piecewise linear fitting to the computed I–V characteristics. Each approach highlights different trade-offs between accuracy, stability, and scalability.

Polynomial fitting provides a smooth global approximation of the I–V curve and achieves higher accuracy as the polynomial order increases (Fig. 3). However, this accuracy comes at the cost of a growing number of coefficients, which not only increases computational complexity but also introduces instability. In particular, high-order polynomials tend to exhibit numerical artifacts such as oscillations or exponential divergence outside the fitted range, leading to poor generalizability. Consequently, while polynomial fitting is precise in theory, its practical utility in scalable implementations is limited by this sensitivity to order and stability.

Alternatively, piecewise linear fitting approximates the nonlinear curve with a set of linear segments, avoiding the instability issues inherent in polynomials (Fig. 4). Although this method may require a denser sampling of bias points to faithfully capture sharp nonlinear features, it provides a more stable and interpretable representation. Importantly, its segment-wise construction makes it readily extensible to larger systems and suitable for practical implementations where robustness is critical. To further ensure stability, current values beyond the simulated voltage range were fixed to the corresponding boundary values. This treatment prevented unphysical exponential divergence in extrapolated regions, thereby maintaining the reliability of the fitted models.

The I–V characteristics of these devices, along with their corresponding piecewise linear fitting results, are presented in Fig. 4. Besides, current values beyond the simulation boundaries were fixed to the values at the boundary points in order

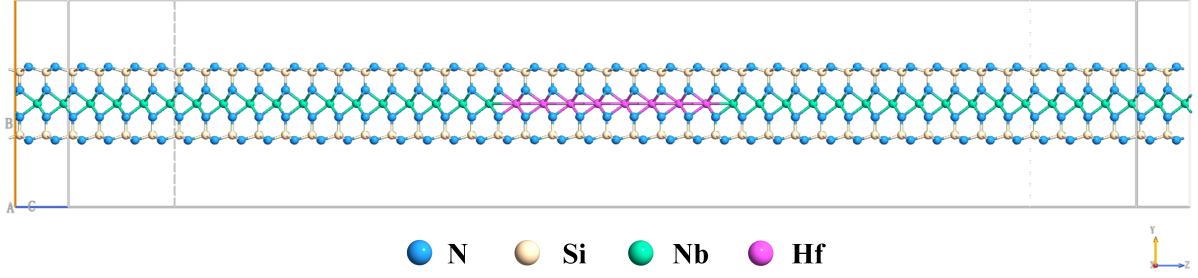


Fig. 2: Schematic illustration of the atomic structure of the $\text{NbSi}_2\text{N}_4/\text{HfSi}_2\text{N}_4/\text{NbSi}_2\text{N}_4$ lateral heterojunction tunnel diode device in armchair orientation, the tunnel barrier width is 21 Å.

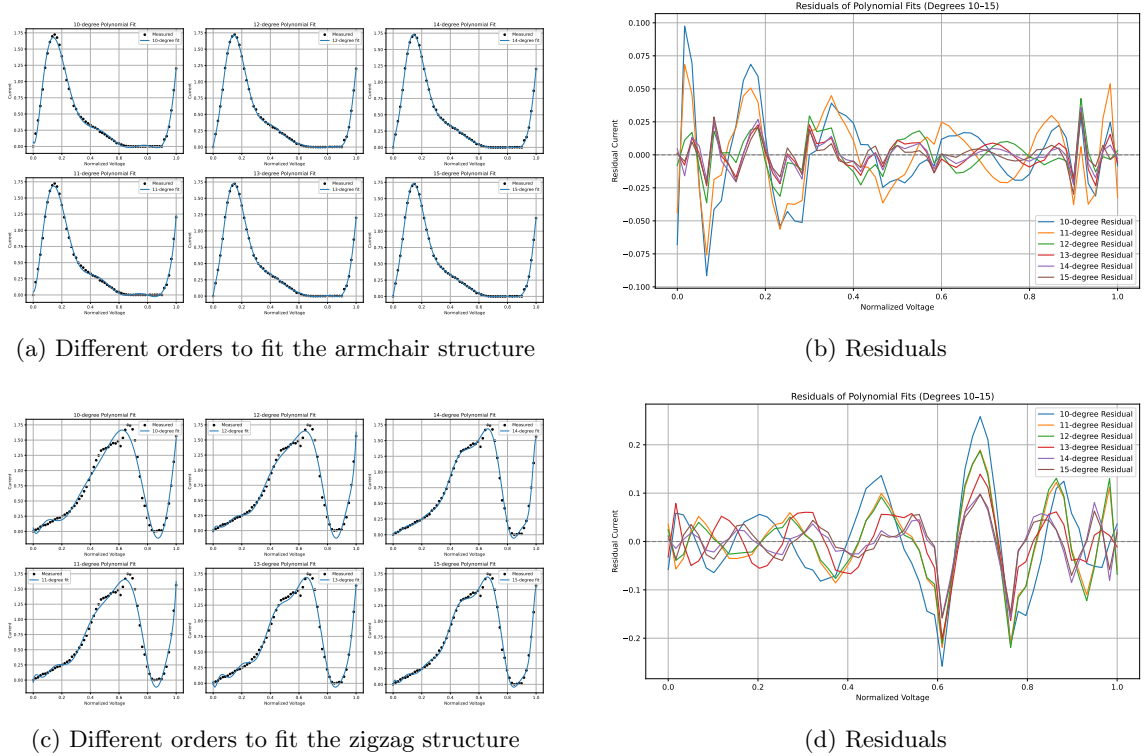
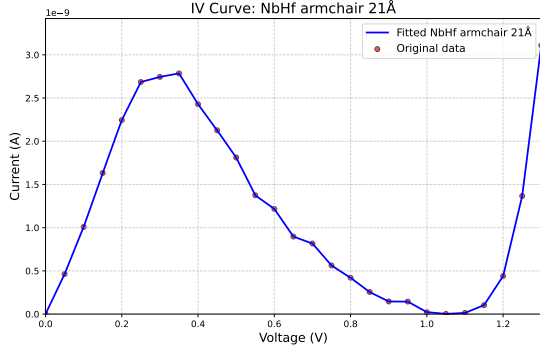


Fig. 3: Polynomial Fitting results and residuals for the I-V characteristics. The polynomial fitting exhibits relatively large residuals near extrema, making it less effective in capturing all of the fine details of the curve.

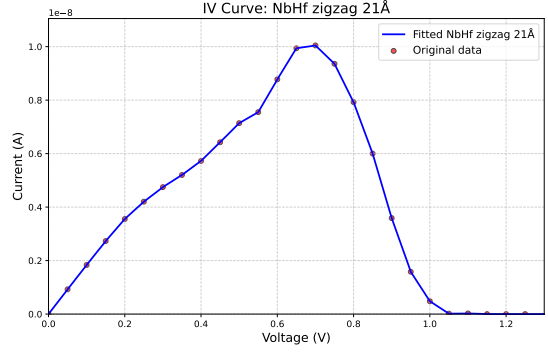
to prevent numerical instabilities such as exponential divergence outside the range of computed voltages.

Overall, these results indicate that piecewise linear fitting offers a stable and scalable approximation scheme, whereas polynomial fitting, despite its accuracy, suffers from instability

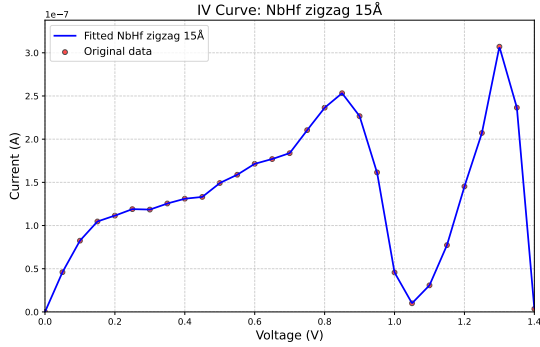
that can hinder its application. From the perspective of neural network design, this distinction is critical: piecewise functions provide a robust basis for implementing device-inspired activation functions in KAN or MLP frameworks, while polynomial-based functions, though expressive,



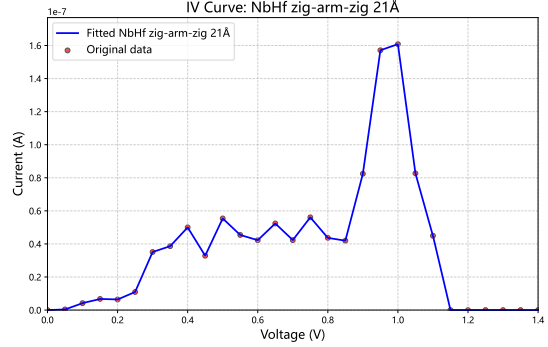
(a) Piecewise fitting for armchair 21 Å



(b) Piecewise fitting for zigzag 21 Å



(c) Piecewise fitting for zigzag 15 Å



(d) Piecewise fitting for zig-arm-zig 21 Å

Fig. 4: Piecewise fitting results for the four different structure.

risk undermining training stability due to their numerical fragility.

3.3 Benchmark Performance of KANalog

We evaluate the performance of KANalog on standard image classification tasks, including MNIST, FashionMNIST, and CIFAR-10. Our focus is to assess: (1) the impact of different tunnel diode combination, (2) the benefit of including bias terms, and (3) generalization across datasets.

3.3.1 MNIST

We first train KANalog on the MNIST dataset using a two-layer architecture with hidden dimension 64. In Fig. 5, we compare models using different combination of tunnel diode functions, such as only armchair 21 Å or armchair 21 Å & zigzag 21 Å. Models with more tunnel diode functions

generally perform better, due to rich nonlinear ability.

Finally, we perform a hyperparameter sweep across learning rates, batch sizes, and hidden dimensions. We choose best performance combination A21+Z21+ZAZ21. Results are summarized in supplement Fig. A5, showing that moderate learning rates and middle-sized hidden layers strike the best trade-off between accuracy and training efficiency.

3.3.2 FashionMNIST

We extend our evaluation to the more challenging FashionMNIST dataset using a two-layer KAN model with a hidden dimension of 256. Figs. 6 and A6 replicate the experiments from MNIST.

3.3.3 CIFAR-10

We test the generalization of KANalog on CIFAR-10 using a deeper architecture with a 512-dim hidden layer. As Figs. 7 and A7 shown below,

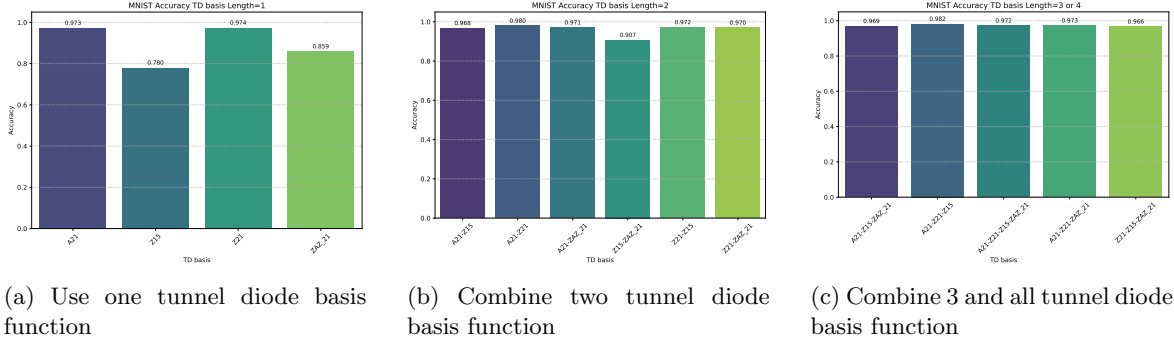


Fig. 5: On the MNIST dataset. The KAN model uses a 64-dimensional hidden layer, batch size 64, cross-entropy loss, Adam optimizer with learning rate 0.001, trained for 10 epochs. MNIST images are resized to 14×14 and enhanced with $\lambda = 2.5$. As order increases, accuracy tends to decrease—possibly due to increasing weight complexity.

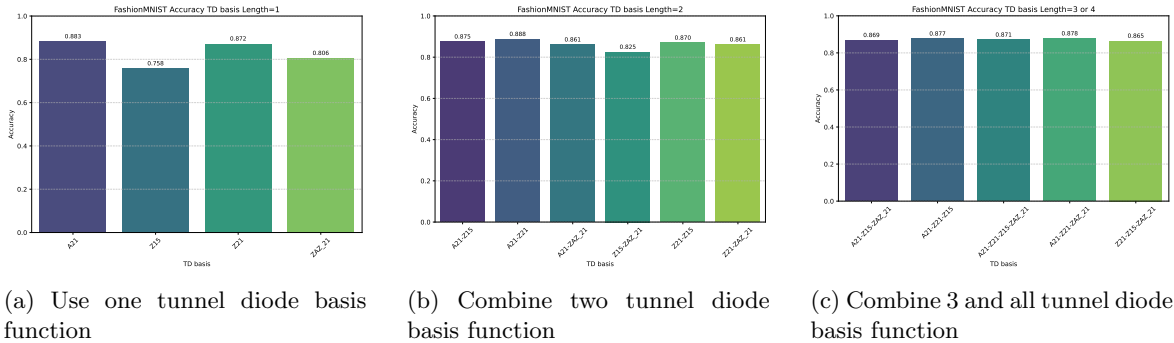


Fig. 6: On the FashionMNIST dataset.

accuracy peaks below 50%, suggesting that the current polynomial-fitted tunnel diode basis may not scale well to complex natural images. Improving basis flexibility or adding learnable tuning parameters could address this gap in future work.

3.4 Robustness to coefficient perturbations

To evaluate the robustness of tunnel-diode KANs against parameter variations, we introduced relative errors into the trained coefficient tensors and measured the resulting classification accuracy. Specifically, multiplicative perturbations of the form

$$\tilde{\Theta}_{i,j,k} = \Theta_{i,j,k}(1 + \delta), \quad (6)$$

were applied during inference, where δ denotes a random variable sampled from a zero-mean distribution with a specified relative error magnitude.

This perturbation mimics inaccuracies that may arise in physical implementations due to device mismatch or fabrication imperfections.

Figure 8 shows the test accuracy as a function of the relative error level for networks with different parameter counts. As expected, larger relative errors lead to a gradual decrease in accuracy. However, we observed that models with more parameters exhibit significantly greater tolerance to perturbations: the accuracy degradation becomes less pronounced as the network size increases. This trend indicates that overparameterization not only improves expressivity but also enhances error resilience, allowing the network to compensate for perturbations through redundancy in the learned basis expansions.

These results suggest that scaling up tunnel-diode KAN architectures could provide a practical

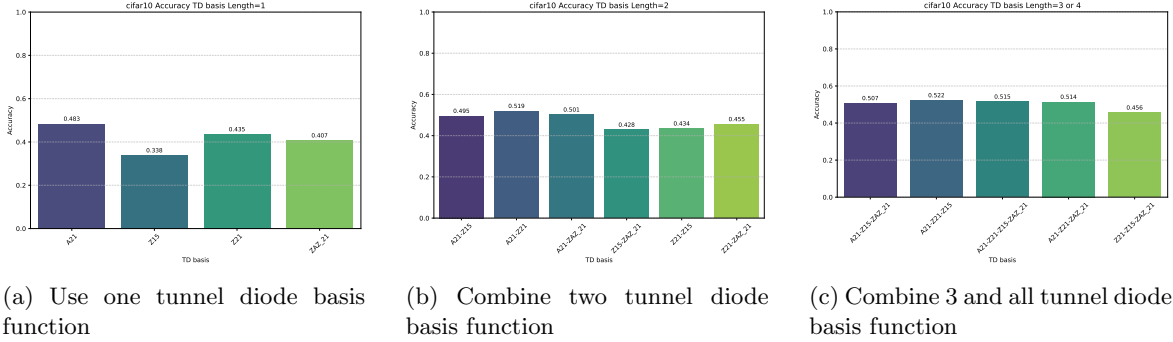


Fig. 7: On the cifar-10 dataset.

pathway toward robust analog neural computation, where inevitable device-level fluctuations are mitigated by the inherent redundancy of the network.

3.5 Comparison with MLP and KAN

To further evaluate the performance of our proposed network, we compared it directly against the original KAN and a conventional MLP on the MNIST handwritten digit recognition benchmark. This comparison allows us to assess not only the absolute classification accuracy but also the relative advantages in terms of training stability, representational efficiency, and the ability to capture nonlinear features. By positioning our model alongside both the widely used MLP and the emerging KAN framework, we establish a clear baseline for quantifying the improvements introduced by our design.

3.5.1 MLP

We first evaluated the performance of the TD function within a conventional MLP framework. Traditional MLP architectures typically employ standard activation functions such as ReLU or Sigmoid. In our work, we adopted the I–V curve of our own cold-metal tunnel diode with an armchair 21 Å barrier as a replacement activation function (Cold Metal Tunnel Diode Activate Function, CMTDAF).

For the choice of nonlinear activation functions in the MLP, we additionally included a resonant tunneling diode (RTD) and an E-MOSFET for comparison, while the classical ReLU and Sigmoid

functions were also considered. The results are shown in Fig. 9.

3.5.2 Origin KAN

We test origin KAN in MNIST dataset. We employed B-spline functions and Gottlieb polynomial as basis functions. The B-spline function use the De Boor-Cox recursive formula to generate higher-order spline basis functions. To reduce the number of parameters in the model, we set the grid size of spline for each input dimension to three and used B-splines of order two. Similarly, the Gottlieb polynomial use 1-3 orders of generate [37].

3.5.3 Comparison Table

To further assess the advantages of KAN over conventional MLPs, we conducted systematic comparisons across three benchmark datasets: MNIST, FashionMNIST, and CIFAR-10. Two complementary perspectives were considered. First, we compared MLP and KAN under identical architectural settings, thereby isolating the effect of replacing fixed activation functions with basis functions. Second, we compared the two models when matched by a similar number of trainable parameters, providing a fair evaluation of model efficiency. The results, summarized in Table 1, consistently highlight the superior competitive parameter efficiency of KANanlog.

4 Discussion

Our results demonstrate that embedding tunnel-diode nonlinearities into Kolmogorov–Arnold Networks offers a viable pathway toward fully analog

Table 1: Comparison of MLP and KAN with the same architectures on MNIST, FashionMNIST and cifar-10

Dataset	Network	Architecture	#Params	Accuracy (%)
MNIST	MLP(RTDAF)	[196, 64, 10]	13,258	97.58
MNIST	MLP(CMTDAF)	[196, 64, 10]	13,258	97.04
MNIST	MLP(E-MOSFET)	[196, 64, 10]	13,258	97.00
MNIST	KAN(B-splines)	[196, 64, 10]	92,288	97.78
MNIST	KAN(Gottlieb)	[196, 64, 10]	52,866	97.47
MNIST	KANanlog(2 basis)	[196, 64, 10]	26,570	97.71
MNIST	KANanlog(3 basis)	[196, 64, 10]	39,754	97.04
FashionMNIST	MLP(RTDAF)	[784, 256, 10]	203,530	94.28
FashionMNIST	MLP(CMTDAF)	[784, 256, 10]	203,530	94.84
FashionMNIST	MLP(E-MOSFET)	[784, 256, 10]	203,530	91.38
FashionMNIST	KAN(B-splines)	[784, 256, 10]	1,219,584	96.32
FashionMNIST	KAN(Gottlieb)	[784, 256, 10]	813,570	93.44
FashionMNIST	KANanlog(2 basis)	[784, 256, 10]	407,306	89.08
FashionMNIST	KANanlog(3 basis)	[784, 256, 10]	610,570	88.89
cifar-10	MLP(RTDAF)	[3072, 1024, 256, 10]	3,411,722	51.90
cifar-10	MLP(CMTDAF)	[3072, 1024, 256, 10]	3,411,722	34.13
cifar-10	MLP(E-MOSFET)	[3072, 1024, 256, 10]	3,411,722	26.64
cifar-10	KAN(B-splines)	[3072, 1024, 256, 10]	20,462,592	57.10
cifar-10	KAN(Gottlieb)	[3072, 1024, 256, 10]	13,644,291	45.71
cifar-10	KANanlog(2 basis)	[3072, 1024, 256, 10]	10,233,856	50.27
cifar-10	KANanlog(3 basis)	[3072, 1024, 256, 10]	13,644,288	48.55

learning systems. By directly mapping device-level current–voltage responses to univariate basis functions, KANalog circumvents the need for digitally implemented activations and establishes a compact representation that scales naturally with hardware. This co-design across quantum transport physics and learning architectures illustrates how computational science can integrate materials modeling, circuit behavior, and algorithmic function approximation.

At the device level, our simulations leverage that structural variations, such as armchair or zigzag orientations and barrier thickness tuning, yield qualitatively distinct nonlinear current–voltage characteristics. These differences translate directly into a richer family of basis functions for KANs representations, grounding functional diversity in atomic-scale physics. Taken

together, these findings position tunnel diodes not only as feasible intrinsic nonlinear activations but also as practical building blocks for modular, energy-efficient analog machine learning systems that connect quantum transport phenomena with algorithmic expressivity.

Despite these promising results, several limitations remain. Current evaluations are based on simulated current–voltage curves and surrogate fits, which may not capture all fabrication-level imperfections. Performance on more complex datasets, such as CIFAR-10, also indicates a scalability bottleneck arising from limited functional diversity in fixed diode responses. Practical deployment will require careful circuit-level co-design to address device mismatch, thermal drift, and noise, as well as strategies for adaptive or

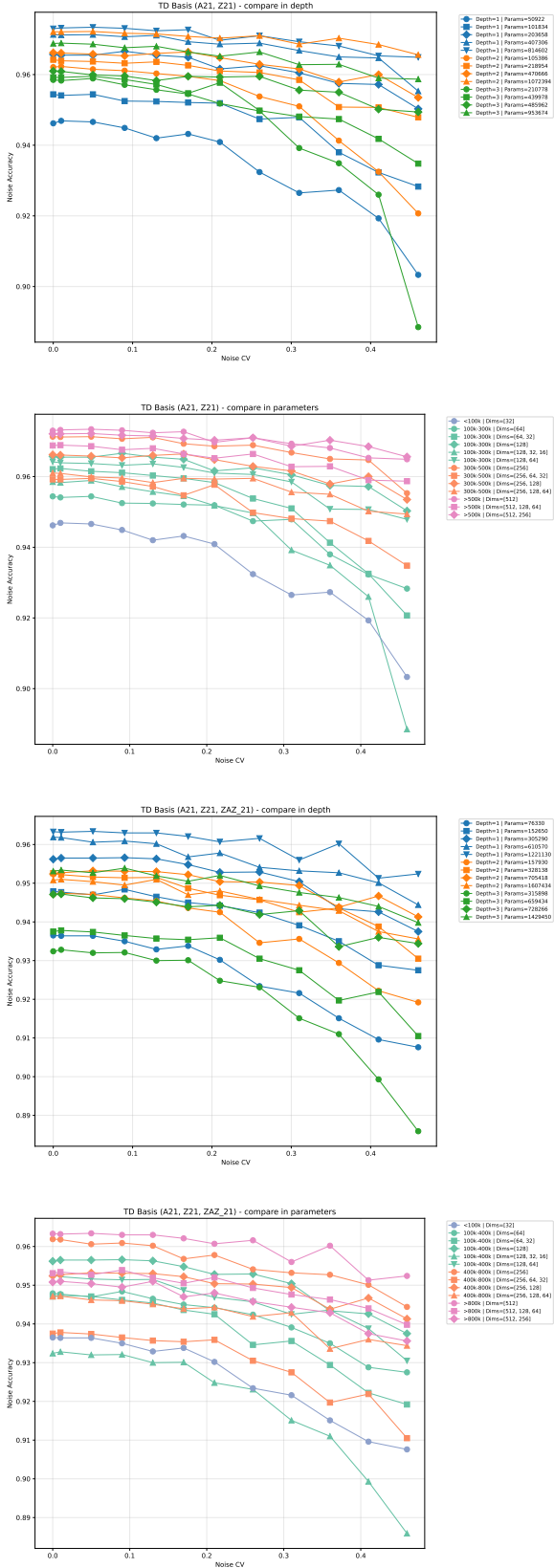


Fig. 8: Relative Noise Error Comparison in similar depth or parameters 11

programmable nonlinearities to support continual learning.

Looking forward, fabricating tunnel-diode arrays and characterizing their collective behavior will be critical to establish experimental viability and enable direct benchmarking of energy efficiency. Embedding KANalog into larger neuromorphic or edge-computing pipelines would further validate its relevance in real-world, resource-constrained environments. More broadly, this work points toward a new class of analog-compatible learning architectures with interpretable and modular function representations, opening avenues for compact neuromorphic hardware that unifies device physics with functional learning theory.

5 Conclusion

We have introduced KANalog, a novel framework that bridges Kolmogorov–Arnold Networks (KANs) with analog nonlinear devices through a physically grounded implementation of univariate basis functions. By mapping trainable functions in KANs to the I–V characteristics of tunnel diodes, KANalog offers a hardware-efficient alternative to traditional digital neural architectures. Our experiments on MNIST and FashionMNIST demonstrate that KANalog achieves competitive accuracy while substantially reducing model complexity and enabling direct physical realizability. Through extensive ablation studies, we show how structural configurations (e.g., armchair vs. zigzag orderings) and bias parameterizations influence learning dynamics and performance. This work establishes a new direction toward analog-compatible learning architectures with interpretable and modular function representations, opening the door to future integration of compact neuromorphic hardware and function-based learning.

References

- [1] Friz, A. *et al.* An analog-ai chip for energy-efficient speech recognition and transcription. *Nature* **620**, 768–775 (2023).
- [2] Wen, T.-H. *et al.* Fusion of memristor and digital compute-in-memory processing

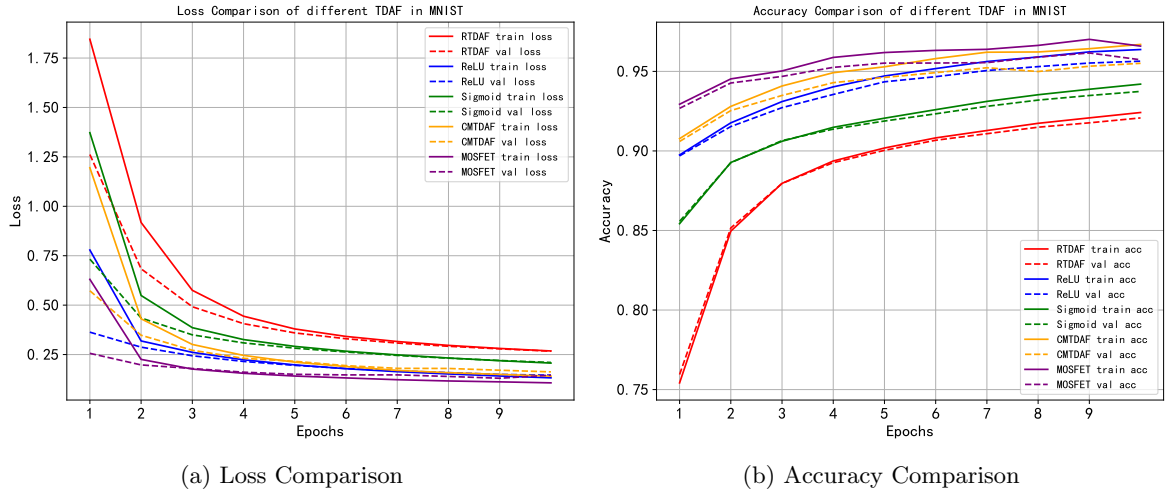


Fig. 9: Comparison of different activation function.

- for energy-efficient edge computing. *Science* **384**, 325–332 (2024).
- [3] Mead, C. Neuromorphic electronic systems. *Proceedings of the IEEE* **78**, 1629–1636 (1990).
- [4] Kudithipudi, D. *et al.* Neuromorphic computing at scale. *Nature* **637**, 801–812 (2025).
- [5] Büchel, J. *et al.* Kernel approximation using analogue in-memory computing. *Nature Machine Intelligence* **6**, 1605–1615 (2024).
- [6] Huang, Y. *et al.* Memristor-based hardware accelerators for artificial intelligence. *Nature Reviews Electrical Engineering* **1**, 286–299 (2024).
- [7] Zhang, C., Li, Y., Lin, Y. & Wang, Y. A computing-in-memory macro based on three-dimensional resistive random-access memory. *Nature Electronics* **4**, 291–299 (2021).
- [8] Le Gallo, M., Khaddam-Aljameh, R., Stanisavljevic, M. *et al.* A 64-core mixed-signal in-memory compute chip based on phase-change memory for deep neural network inference. *Nature Electronics* **6**, 680–693 (2023).
- [9] Rasch, M. J., Carta, F., Fagbohunge, O. & Gokmen, T. Fast and robust analog in-memory deep neural network training. *Nature Communications* **15**, 7133 (2024).
- [10] Aguirre, F. *et al.* Hardware implementation of memristor-based artificial neural networks. *Nature communications* **15**, 1974 (2024).
- [11] Wu, Z., Gokmen, T., Rasch, M. J. & Chen, T. Towards exact gradient-based training on analog in-memory computing (2024).
- [12] Lanza, M. *et al.* The growing memristor industry. *Nature* **640**, 613–622 (2025).
- [13] Wang, S. *et al.* Echo state graph neural networks with analogue random resistive memory arrays. *Nature Machine Intelligence* **5**, 104–113 (2023).
- [14] Sebastian, A., Le Gallo, M., Khaddam-Aljameh, R. & Eleftheriou, E. Memory devices and applications for in-memory computing. *Nature nanotechnology* **15**, 529–544 (2020).
- [15] Xi, Y. *et al.* In-memory learning with analog resistive switching memory: A review and perspective. *Proceedings of the IEEE* **109**, 14–42 (2020).

- [16] Seok, H. *et al.* Beyond von neumann architecture: Brain-inspired artificial neuromorphic devices and integrated computing. *Advanced Electronic Materials* **10**, 2300839 (2024).
- [17] Yang, J., Mao, R., Jiang, M. *et al.* Efficient nonlinear function approximation in analog resistive crossbars for recurrent neural networks. *Nature Communications* **16**, 1136 (2025).
- [18] Kolmogorov, A. N. On the representations of continuous functions of many variables by superposition of continuous functions of one variable and addition **114**, 953–956 (1957).
- [19] Liu, Z. *et al.* KAN: Kolmogorov–arnold networks N/A (2025).
- [20] SS, S., AR, K., R, G. & KP, A. Chebyshev polynomial-based kolmogorov-arnold networks: An efficient architecture for nonlinear function approximation. arXiv preprint arXiv:2405.07200 (2024). URL <https://arxiv.org/abs/2405.07200>.
- [21] Aghaei, A. A. fkan: Fractional kolmogorov–arnold networks with trainable jacobi basis functions. *Neurocomputing* **623**, 129414 (2025).
- [22] Bozorgzadeh, Z. & Chen, H. Wav-kan: Wavelet kolmogorov–arnold networks. arXiv preprint arXiv:2405.12832 (2024). URL <https://arxiv.org/abs/2405.12832>.
- [23] Toscano, J. D., Wang, L.-L. & Karniadakis, G. E. Kkans: Kůrkova–kolmogorov–arnold networks and their learning dynamics. arXiv preprint arXiv:2412.16738 (2024). URL <https://arxiv.org/abs/2412.16738>.
- [24] Cheon, M. Kolmogorov-arnold network for satellite image classification in remote sensing. *arXiv preprint arXiv:2406.00600* (2024). URL <https://arxiv.org/abs/2406.00600>.
- [25] Li, L., Zhang, Y., Wang, G. & Xia, K. Kolmogorov–arnold graph neural networks for molecular property prediction. *Nature Machine Intelligence* 1–9 (2025).
- [26] Huang, W.-H. *et al.* Hardware acceleration of kolmogorov-arnold network (kan) for lightweight edge inference 693–699 (2025).
- [27] Peng, Y. *et al.* Photonic kan: A kolmogorov–arnold network inspired efficient photonic neuromorphic architecture. *arXiv preprint arXiv:2408.08407* (2024). URL <https://arxiv.org/abs/2408.08407>.
- [28] Esaki, L. New phenomenon in narrow germanium p-n junctions. *Physical review* **109**, 603 (1958).
- [29] Tsu, R. & Esaki, L. Tunneling in a finite superlattice. *Applied Physics Letters* **22**, 562–564 (1973).
- [30] Chang, L., Esaki, L. & Tsu, R. Resonant tunneling in semiconductor double barriers. *Applied physics letters* **24**, 593 (1974).
- [31] Şaşıođlu, E. & Mertig, I. Theoretical prediction of semiconductor-free negative differential resistance tunnel diodes with high peak-to-valley current ratios based on two-dimensional cold metals. *ACS Applied Nano Materials* **6**, 3758–3766 (2023).
- [32] Bodewei, Z., Huang, Z., Sun, L., Yu, Z. & Yu, G. Computational design of tunnel diodes with negative differential resistance and ultrahigh peak-to-valley current ratio based on two-dimensional cold metals. *Physical Review Applied* **22**, 014004 (2024). URL <https://doi.org/10.1103/PhysRevApplied.22.014004>.
- [33] Donati, G., Owen-Newns, D., Robertson, J., Malysheva, E. *et al.* Spiking flip-flop memory in resonant tunneling diode neurons. *Physical Review Letters* **133**, 267301 (2024).
- [34] McNaughton, J., Abbas, A. H. & Maksymov, I. S. Neuromorphic quantum neural networks with tunnel-diode activation functions. *arXiv preprint arXiv:2503.04978* (2025). URL <https://arxiv.org/abs/2503.04978>.
- [35] Ortega-Piwonka, I., Piro, O., Figueiredo, J., Romeira, B. & Javaloyes, J. Bursting and

excitability in neuromorphic resonant tunneling diodes. *Physical Review Applied* **15**, 034017 (2021).

[36] Smidstrup, S. *et al.* Quantumatk: an integrated platform of electronic and atomic-scale modelling tools. *Journal of Physics: Condensed Matter* **32**, 015901 (2019).

[37] Seydi, S. T. Exploring the potential of polynomial basis functions in kolmogorov-arnold networks: A comparative study of different groups of polynomials. arXiv preprint arXiv:2406.02583 (2024). URL <https://arxiv.org/abs/2406.02583>.

Appendix A **Supplementary information**

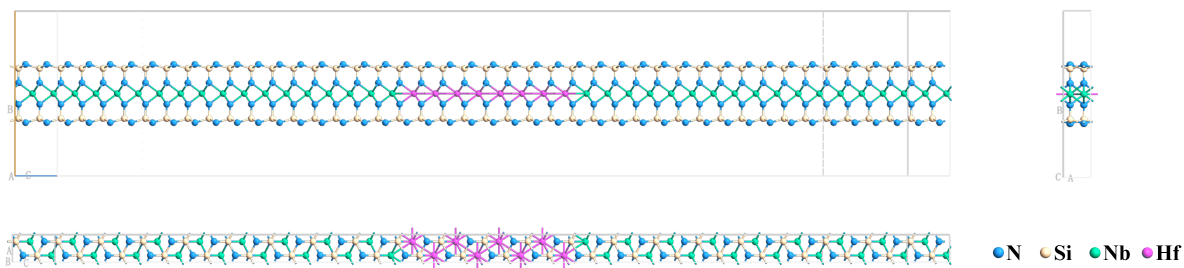


Fig. A1: Three-view and overview drawing of tunnel diode in armchair orientation. The tunnel barrier width is 21 Å.

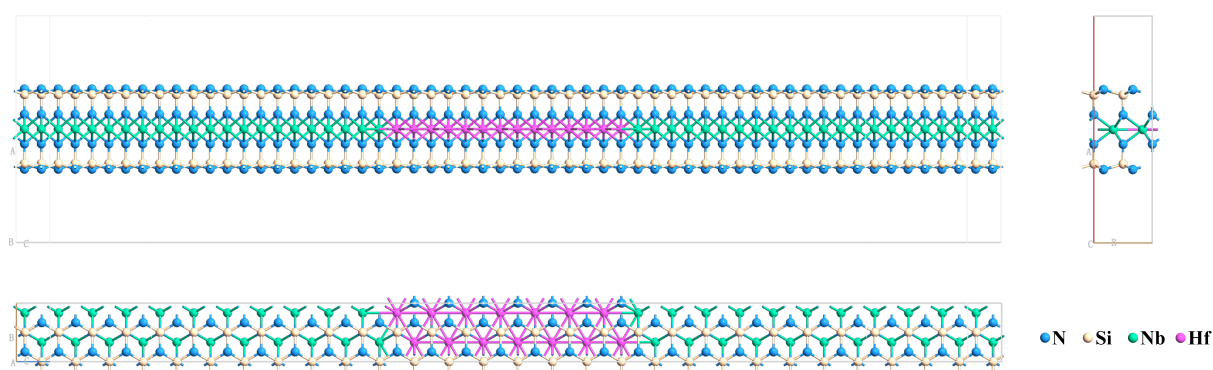


Fig. A2: Three-view and overview drawing of tunnel diode in zigzag orientation. The tunnel barrier width is 21 Å.

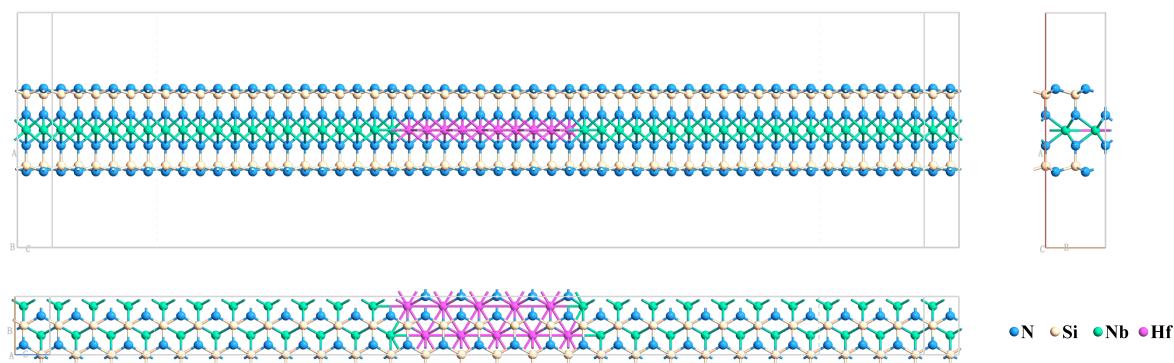


Fig. A3: Three-view and overview drawing of tunnel diode in armchair orientation. The tunnel barrier width is 15 Å.

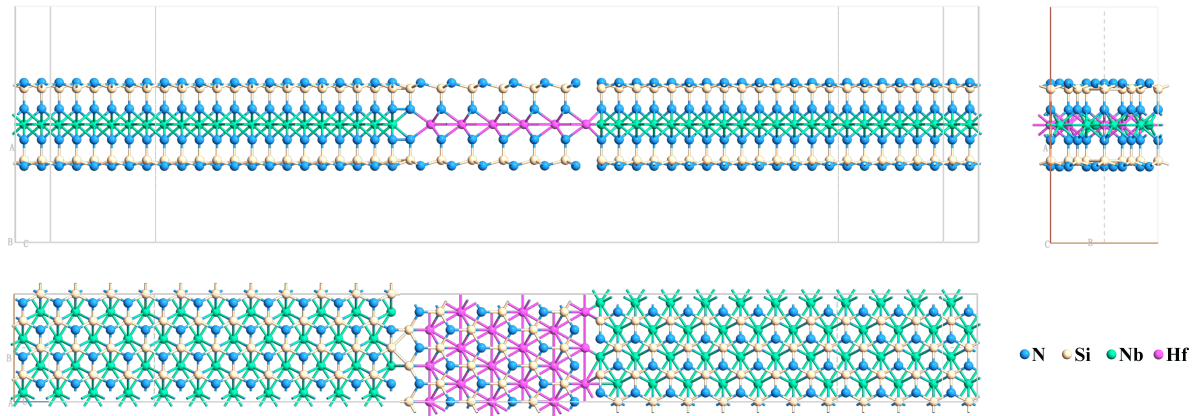


Fig. A4: Three-view and overview drawing of hybrid structure tunnel diode. The tunnel barrier width is 21 Å.

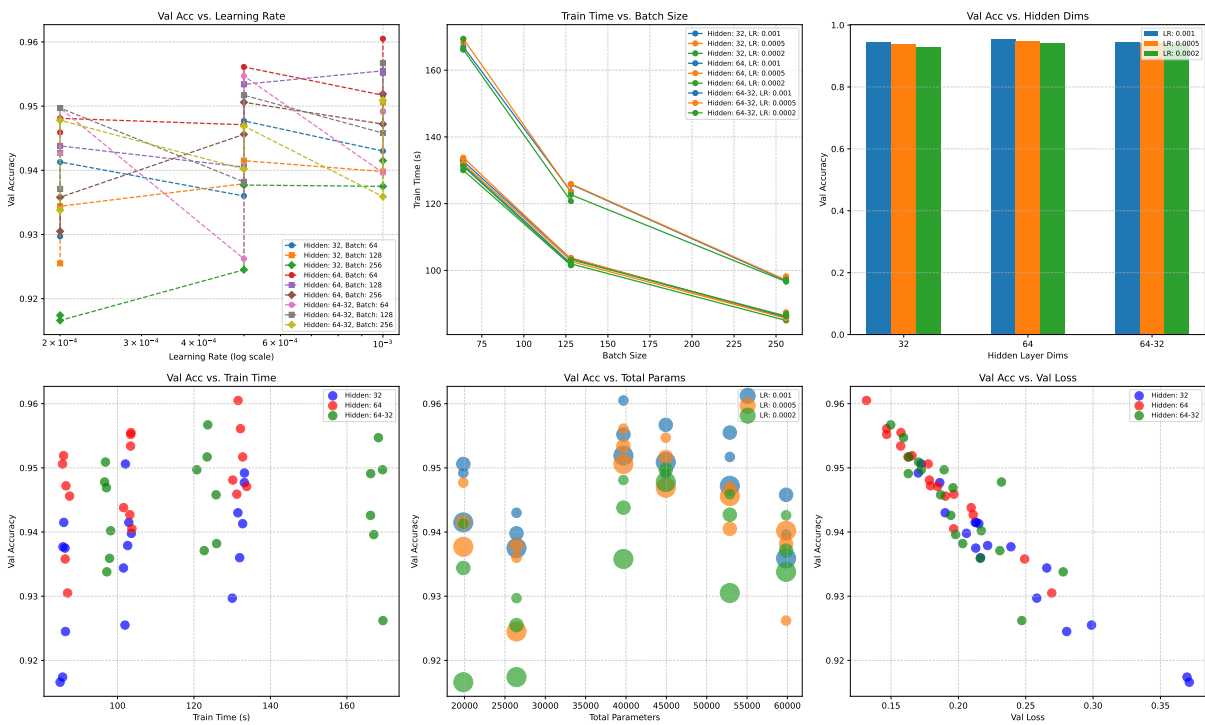


Fig. A5: hyper parameter test in MNIST We compare different usual parameters, like 0.0004, 0.0002, 0.0001 learning rate; 32, 64, 128 batch size; [32], [64], [64, 32] hidden dims.

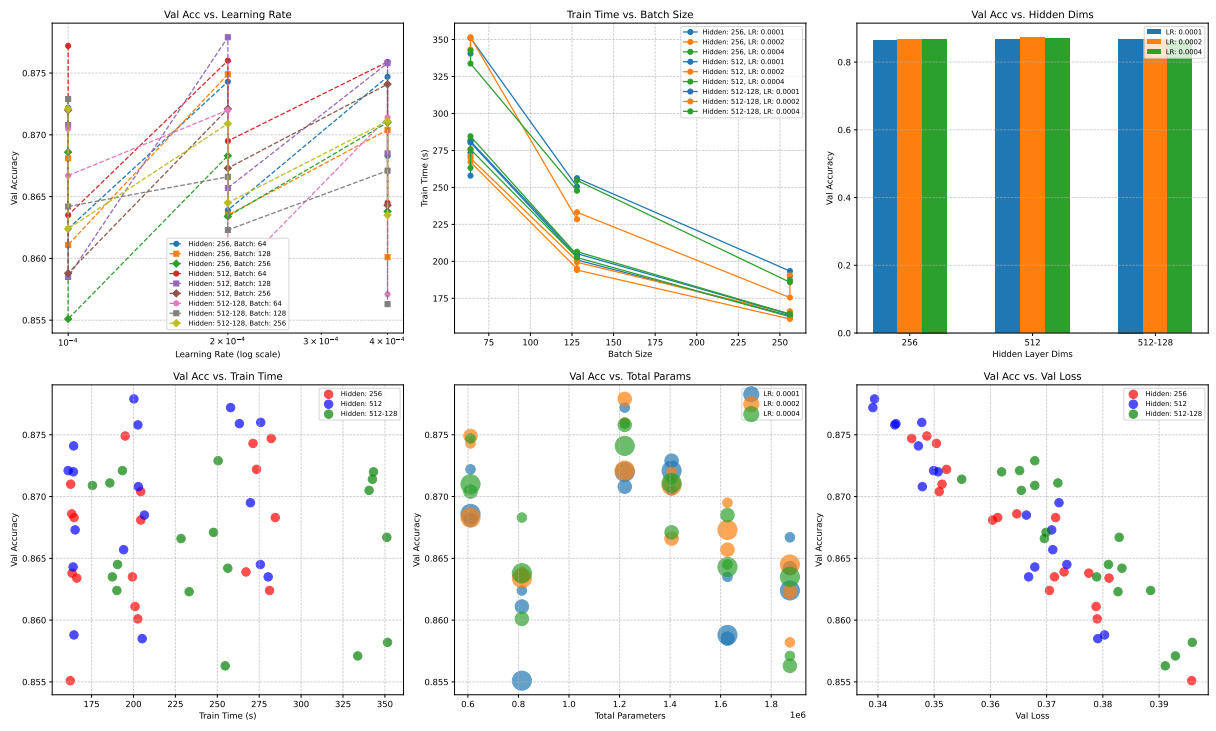


Fig. A6: hyper parameter test in FashionMNIST We different usual parameters, like 0.0004, 0.0002, 0.0001 learning rate; 64, 128, 256 batch size; [256], [512], [512, 128] hidden dims.

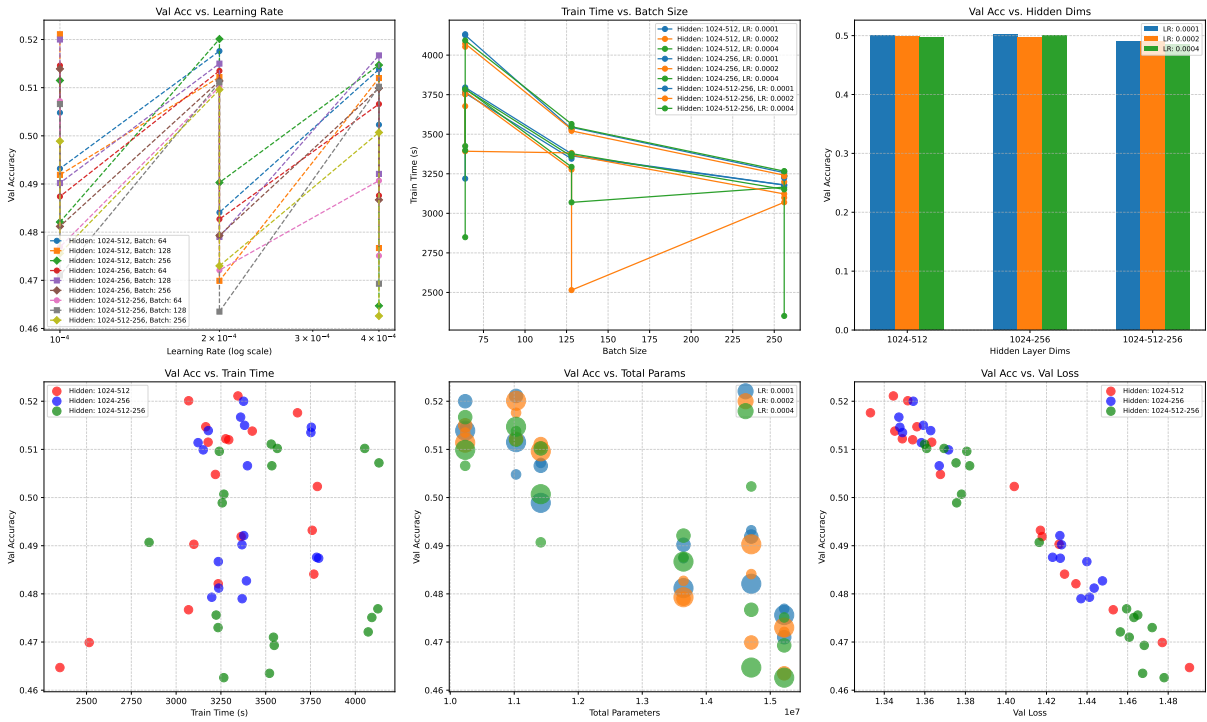


Fig. A7: hyper parameter test in cifar10 We compare different usual parameters, like 0.0004, 0.0002, 0.0001 learning rate; 64, 128, 256 batch size; [1024, 512], [1024, 256], [1024, 512, 256] hidden dims.